Available online at www.sciencedirect.com

SCIENCE DIRECT®

Journal of Solid State Chemistry 179 (2006) 233–246

JOURNAL OF SOLID STATE CHEMISTRY

www.elsevier.com/locate/jssc

# Zirconium titanate ceramic pigments: Crystal structure, optical spectroscopy and technological properties

M. Dondi[a], F. Matteucci[a,*], G. Cruciani[b]

[a]Institute of Science and Technology for Ceramics (ISTEC–CNR), Via Granarolo 64, 48018 Faenza, Italy
[b]Department of Earth Sciences, Via Saragat 1, University of Ferrara, 44100 Ferrara, Italy

Received 16 August 2005; received in revised form 14 October 2005; accepted 16 October 2005
Available online 5 December 2005

## Abstract

Srilankite-type zirconium titanate, a promising structure for ceramic pigments, was synthesized at 1400 °C following three main doping strategies: (a) $ZrTi_{1-x}A_xO_4$, (b) $ZrTi_{1-x-y}A_xB_yO_4$ and (c) $Zr_{1-x}C_xTiO_4$ where $A =$ Co, Cr, Fe, Mn, Ni or V (chromophores), $B =$ Sb or W (counterions) and $C =$ Pr (chromophore); $x = y = 0.05$. Powders were characterized by XRD with Rietveld refinements and DRS in the UV–visible–NIR range; technological properties were appraised in several ceramic matrices (frits, glazes and body). Zirconium titanate can be usefully coloured with first row transition elements, giving green and greenish yellow (Co and Ni); orange-buff (Cr and V); tan-brown hues (Mn and Fe). In industrial-like synthesis conditions, a disordered structure as $(Zr,Ti)O_2$, with both Zr and Ti randomly distributed in the octahedral site, is achieved. Doping with chromophores and counterions induces unit cell dimensions variation and causes an oversaturation in zirconium oxide. Optical spectroscopy reveals the occurrence of $Co^{2+}$, $Cr^{3+}$, $Fe^{3+}$, $Mn^{2+}$, $Mn^{3+}$, $Ni^{2+}$, $V^{3+}$ and $V^{4+}$. The zirconium titanate pigments fulfil current technological requirements for low-temperature applications, but exhibit a limited chemico-physical stability for higher firing temperature and in chemically aggressive media.

*Keywords:* Ceramic pigments; Crystal structure; Order–disorder; Optical spectroscopy; Zirconium titanate; Srilankite

## 1. Introduction

The zirconium titanate solid solution with Zr:Ti molar ratio ranging from 1:1 to 1:2 is the only stable binary compound in the Zr–Ti–O system [1]. Two structural modifications are known: high-temperature disordered $Zr_{1-x}Ti_xO_4$ and low-temperature ordered $ZrTiO_4$ [2–4]. The high-T disordered phase crystallizes in the orthorhombic $\alpha$-$PbO_2$ structure (space group *Pbcn*; setting of the unit cell: $a \cdot b \cdot c = 4.7 \cdot 5.5 \cdot 5.0$ Å; Zr and Ti randomly distributed in the octahedral site with $0.41 < X_{Ti} < 0.53$ at 1400 °C [3,4]). This phase is stable above 1100 °C and persists metastably at lower temperature because the ordering process is sluggish, being associated with a reconstructive transformation and driven by the respective preferences of the Zr and Ti ions for 8(7)- and sixfold coordination, respectively [3,4]. There are two types of ordered structures with different stoichiometries both stable below 1200 °C [5,6]:

- stacking of two layers of distorted Zr sites plus two layers of octahedral Ti sites alternated along the axis $a$, giving rise to a doubling of the parameter $a$ (cell setting: $a \cdot b \cdot c = 9.6 \cdot 5.3 \cdot 5.0$ Å) with respect to the disordered phase; this ordering scheme is consistent with the formula $ZrTiO_4$ (Zr:Ti ratio = 1:1; $X_{Ti} = 0.5$);
- Zr is hosted onto one every three cation layer (Zr site approaches eightfold coordination) so that the parameter $a$ is threefold (cell setting: $a \cdot b \cdot c = 14.4 \cdot 5.3 \cdot 5.0$ Å) as consistent with the fersmite-type structure $AB_2O_6$; in this case the formula is close to $ZrTi_2O_6$ (Zr:Ti = 1:2; $X_{Ti} = 0.67$) [3] but the same structure also occurs in $Zr_5Ti_7O_{24}$ (Zr:Ti ratio = 1:1.4) [7].

The mineral srilankite has a composition close to the low-T ordered compound—$ZrTi_2O_6$—but both its natural and synthetic forms were reported to possess the orthor-

---

*Corresponding author. Fax. +39 546 46381.
*E-mail address:* matteucci@istec.cnr.it (F. Matteucci).

0022-4596/$ - see front matter © 2005 Elsevier Inc. All rights reserved.
doi:10.1016/j.jssc.2005.10.032

hombic α-$PbO_2$ structure, thus being isostructural with the high-T disordered polymorph of $(Zr,Ti)_2O_4$ [8,9].

Zirconium titanate exhibits promising characteristics for an application as a ceramic pigment due to its high melting point (~1840 °C), very high refractive indices ($n_x = 2.33$, $n_y = 2.38$, $n_z = 2.41$) and capacity to host into its lattice a large part of the periodic table of elements [10]. Moreover, the presence of a distorted octahedral site with a low point symmetry is favourable to develop intense chromatic effects according to the crystal field (CF) theory [11,12]. However, the variable order/disorder of the structure as well as the changing coordination of zirconium, from an octahedral to a distorted cubic site, are factors whose effects on colouring are unknown.

Zirconium titanate was firstly proposed as ceramic pigment by Hund [10] who designed a huge series of chromophore (i.e. transition elements) + counterion (i.e. ion added to counterbalance the valence mismatch between chromophore and $Ti^{4+}$) combinations in order to test their colouring ability. There have been several reports on the effect of chemical substitutions on the properties of the zirconium titanates [13], but no structural or technological studies are available on these materials, apart a contribution on the isostructural compound $Zr(Ti,Sn)O_4$ [14] and another about a new synthesis route of zirconium titanate pigments [15].

The present study is aimed at synthesizing new ceramic pigments, performing their structural, spectroscopic and technological characterization in order to assess their colourimetric and industrial potentialities.

The design criteria involved the selection of chromophores and counterions utilizable by the ceramic industry for their chemical and technological features (and cost). The chromophores are those currently used to impart colour to Zr- or Ti-bearing pigments, such as rutile (i.e. Cr, Mn, Ni, V) or zircon and baddeleyite (i.e. Fe, Pr, V). Furthermore, Co was chosen for its well-known colouring capacity [16,17].

## 2. Experimental

Along with undoped zirconium titanate, the following formulations were designed according to three different strategies:

- addition of chromophore $A$ in substitution of titanium: $ZrTi_{1-x}A_xO_4$, where $A$ is Co, Cr, Fe, Mn, Ni or V and $x = 0.05$;
- $ZrTi_{1-x-y}A_xB_yO_4$, chromophore $A$ (i.e. Co, Cr, Fe, Mn, Ni, or V) is introduced together with a counterion $B$ (Sb or W) in the same amount ($x = y = 0.05$) in replacement of titanium, in order to promote a charge balance of the structure;
- $Zr_{1-x}Pr_xTiO_4$, by replacing Pr after zirconium ($x = 0.05$).

These samples are named hereafter with symbols of the chromophore and counterion added. Therefore, the series doped with the chromophore only and with the chromophore plus counterion are named with C and C+C, respectively. The undoped zirconium titanate is called 'ZT'.

Reagent-grade oxides of anatase ($TiO_2$), baddeleyite ($ZrO_2$), chromophores ($Co_3O_4$, $Cr_2O_3$, $Fe_2O_3$, $Mn_2O_3$, NiO, $Pr_6O_{11}$, $V_2O_5$) and counterions ($Sb_2O_3$, $WO_3$) were used as raw materials. No mineralizer was added.

The pigments were synthesized by the conventional ceramic process: wet mixing of raw materials in porcelain jar with alumina grinding media, drying in oven at 105 °C, pulverization in agate mortar, then calcination in alumina crucibles in an electric kiln in static air at maximum temperature of 1400 °C, with thermal rate of 200 °C/h, annealing time (permanence at the maximum temperature) of 1 h and natural cooling to room temperature.

The calcined samples, previously dry ground in an agate mortar and sieved below 50 μm, were characterized by structural, spectroscopic and technological viewpoints.

X-ray powder diffraction was performed by a Philips PW1820/00 goniometer using graphite-monochromated Cu $K\alpha_{1,2}$ radiation, 15–130 °$2\theta$ measuring range, scan rate 0.02 °$2\theta$, 10 s per step. The structural refinements were performed by the Rietveld method with the GSAS-EXPGUI software package [18,19]. Starting atomic parameters in the *Pbcn* space group for the disordered polymorph of zirconium titanate were taken from Siggel and Jansen [14] and used for all refinements. Amounts of the zirconium titanate and of the accessory phases detected in the synthesis products were also refined. Depending upon the number of impurities, the refined variables ranged up to 52 independent variables including: scale factors, zero-point, 15–21 coefficients of the shifted Chebyschev function to fit the background, zirconium titanate cell dimensions, atomic positions, isotropic displacement parameters and profile coefficients: 1 gaussian ($G_W$) and 2 Lorentzian terms ($L_x$, $L_y$). The number of variables and observations as well as the figures-of-merit of all refinements are summarized in Table 1 and an example of a Rietveld refinement plot is shown in Fig. 1.

UV–visible–NIR spectroscopy was performed by diffuse reflectance with integrating sphere (Perkin Elmer λ35) in the 300–1100 nm range, step 0.3 nm, using $BaSO_4$ as a reference. The positions of the main absorbance peaks in the optical spectra were determined through a deconvolution procedure (PFM, OriginLab), that allowed to obtain averaged values of CF strength ($Dq_{\rm cub}$), peak splitting ($\delta$), crystal field stabilization energy (CFSE), Racah $B_{35}$ parameter and nephelauxetic ratio $\beta_{35}$ (i.e. $B_{35}/B_0$, where $B_{35}$ is experimental and $B_0$ is the value of the free ion [20]). $Dq$ was estimated by the Tanabe–Sugano diagrams and fitting spin-allowed transitions; $B_{35}$ was calculated by spin-allowed transitions [20–22]; $\delta$ was measured as FWHM on some peaks of optical spectra; the CFSE was calculated by $Dq$ values [11].

Technological behaviour was assessed by adding the pigment into different ceramic matrices: porcelain stoneware body (PS); ceramic glazes for floor tiles: porcelain

Table 1
Results of Rietveld refinements of X-ray diffraction patterns of zirconium titanate pigments: number of variables and observations, figures-of-merit, amount of accessory baddeleyite ($ZrO_2$), tialite ($Al_2TiO_5$) and rutile ($TiO_2$)

| Sample | No. of variables | No. of observations | Figures-of-merit | | $ZrO_2$ (wt%) | $Al_2TiO_5$ (wt%) | $TiO_2$ (wt%) |
|---|---|---|---|---|---|---|---|
| | | | $R_F^2$ | $R_{wp}$ | | | |
| ZT | 30 | 228 | 0.05 | 0.14 | 0.0(3) | 0.0(3) | 0.0(1) |
| Co | 43 | 225 | 0.07 | 0.15 | 4.5(5) | 8.1(4) | 0.0(1) |
| CoSb | 30 | 225 | 0.06 | 0.18 | 4.5(3) | 7.4(5) | 0.0(1) |
| CoW | 30 | 226 | 0.11 | 0.24 | 4.7(4) | 1.2(2) | 7.9(4) |
| Cr | 30 | 227 | 0.09 | 0.15 | 0.0(2) | 1.3(4) | 0.0(1) |
| CrSb | 52 | 227 | 0.07 | 0.19 | 0.0(2) | 1.3(3) | 0.0(1) |
| CrW | 32 | 227 | 0.11 | 0.19 | 0.0(2) | 0.0(2) | 0.0(1) |
| Fe | 52 | 226 | 0.07 | 0.17 | 3.8(3) | 4.3(3) | 0.0(1) |
| FeSb | 43 | 226 | 0.06 | 0.17 | 9.1(4) | 7.3(5) | 0.0(1) |
| FeW | 35 | 226 | 0.07 | 0.16 | 3.6(2) | 2.0(3) | 0.0(1) |
| Mn | 50 | 226 | 0.08 | 0.19 | 4.4(3) | 6.3(3) | 0.0(1) |
| MnSb | 40 | 227 | 0.06 | 0.16 | 0.0(2) | 4.5(4) | 0.0(1) |
| MnW | 50 | 226 | 0.07 | 0.18 | 4.5(3) | 2.9(5) | 0.0(1) |
| Ni | 35 | 226 | 0.08 | 0.16 | 0.0(2) | 6.2(4) | 0.0(1) |
| NiSb | 35 | 227 | 0.07 | 0.14 | 0.0(2) | 3.2(5) | 0.0(1) |
| NiW | 35 | 225 | 0.08 | 0.18 | 0.0(2) | 1.3(3) | 3.1(2) |
| V | 40 | 224 | 0.06 | 0.15 | 3.7(3) | 3.4(4) | 0.0(1) |
| VSb | 41 | 226 | 0.06 | 0.17 | 2.3(4) | 3.9(3) | 0.0(1) |
| VW | 40 | 226 | 0.12 | 0.30 | 8.2(4) | 2.6(5) | 8.3(2) |
| Pr | 35 | 227 | 0.08 | 0.11 | 0.0(2) | 3.6(2) | 0.0(1) |

*Note*: Figures in parentheses are standard deviations in the last decimal figure. $R_F^2$ is only referred to zirconium titanate reflections. The number of reflections is referred to zirconium titanate ones.

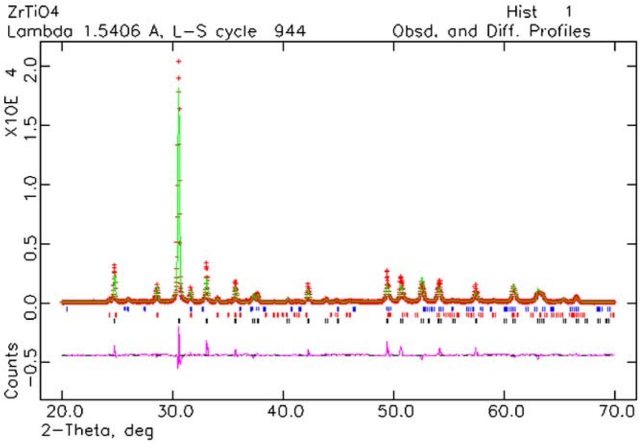

Fig. 1. Rietveld refinement plot of the X-ray powder diffraction data of $ZrTi_{0.95}Co_{0.05}O_4$, where baddeleyite ($ZrO_2$) and tialite ($Al_2TiO_5$) are present as accessory phases. The continuous line represents the calculated pattern, while cross points show the observed pattern. The difference curve between observed and calculated profiles is plotted below.

stonewares S1 and S2; ceramic glaze (S3) and frit (F1) for wall tiles. The pigment addition into the body (3% wt) was carried out by wet mixing, slip drying, powder deagglomeration in agate mortar, hand pelletization (8% wt moisture), uniaxial pressing (40 MPa) of 25 mm-diameter disks, drying in oven (105 °C) and firing in an electric kiln in static air. In the case of glazes and frit, the pigment (5% wt) was wet mixed and the slip was sprinkled on porous ceramic tiles, then dried in oven and fired in an electric kiln in static air. The chemical and physical characteristics of ceramic matrices are reported in Ref. [23]. Both chromatic appearance and colour stability were evaluated by measuring the CIELab parameters $L^*$, $a^*$, $b^*$, and $\Delta E^* = (\Delta L^* + \Delta a^* + \Delta b^*)^{0.5}$ by diffuse reflectance spectroscopy in the visible range (HunterLab Miniscan MSXP4000, 400–700 nm, white glazed tile reference $x = 0.315$, $y = 0.333$). $\Delta E^*$ expresses the total chromatic change with respect to a reference: the lower $\Delta E^*$, the more stable the pigment Table 4.

## 3. Results

### 3.1. X-ray powder diffraction

The undoped zirconium titanate (ZT), as formed in our synthesis conditions, has crystallographic features similar to those of the disordered structure of the high-T polymorph of $ZrTiO_4$, in which Zr and Ti (ratio 1:1) are expected to be randomly distributed in one crystallographically independent octahedral site. Disorder is first indicated by the absence in the XRD patterns of the superstructure reflections which have been observed in the ordered low-T polymorph of $ZrTiO_4$ [3,5]. The *b* dimension of the $ZrTiO_4$ unit cell has been reported to vary from about 5.33 to 5.53 Å as a function of the ordering degree, the largest value being for the more disordered phase [6]. The *b*-axis length refined in our undoped $ZrTiO_4$ sample (5.467 Å) is consistent with an essentially disordered state. The large cooling rate (>100 °C/h), as inferred form the *b*-axis [6], agrees with the evidences that natural cooling (as applied in our process) usually preserves the disordered structure [24–26]. Furthermore, the absence of any $ZrO_2$ phase in the undoped $(Zr,Ti)_2O_4$ sample and the refined occupancy of the octahedral site both indicate a Zr:Ti ratio close to 1:1. On the contrary, all the doped and co-doped samples, except CrW, are not monophasic but present secondary phases such as baddeleyite ($ZrO_2$), rutile ($TiO_2$) and tialite ($Al_2TiO_5$). The latter impurity phase, unexpected from the starting batch composition, is explained by the reaction of $Al_2O_3$, deriving from contamination by alumina grinding media, with $TiO_2$ during calcination. Compared with the undoped sample, both the series C and C+C, show an almost regular decrease of the *b* cell parameter (Fig. 2b), as main contribution to the cell contraction (see also Table 2). At the same time, a moderate and slight increase is observed for the *a* (Fig. 2a) and *c* (Fig. 2c) cell parameters, respectively, the variation of the latter being more regular. Samples V and VW are the only ones showing the *c*-axis smaller than ZT. Despite their regularity, these trends cannot be simply explained on the basis of different ionic size of atoms involved in isomorphous substitutions. As previously discussed, the *b*-axis shortening might be explained by an increased degree of ordering brought about by doping. In fact, it is known that little uncoupled substitutions of trivalent ions (e.g. $Y^{3+}$) for $Zr^{4+}$ are able to enhance the ordering kinetics, presumably through the introduction of oxygen vacancies [13]. Fig. 2b shows that the *b* contraction is actually larger for C series compared to the C+C one. A clear inverse relationship is observed between the *b*-axis length and the amount of baddeleyite ($ZrO_2$) refined in doped and co-doped samples (Fig. 3). This behaviour reveals an increasing departure from the designed Zr:Ti = 1:1 stoichiometry towards the Zr:Ti = 1:1.4 or Zr:Ti = 1:2 molar ratios of the zirconium titanate phase present in the mixture as related to the shortening of the *b*-axis. The presence of small amounts of exsolved $ZrO_2$ was previously reported upon formation of the ordered polymorph of undoped zirconium titanate [2]. Therefore, the increasing excess of $ZrO_2$ can be taken as an additional evidence for the increased degree of ordering of doped and co-doped samples. It should be noted, however, that the presence of the $Al_2TiO_5$ phase in many samples may also be responsible for an excess in $ZrO_2$ likely to crystallize as baddeleyite (Fig. 4). The refined occupancies in the octahedral site (Table 2) are consistent with the Ti enrichment of the zirconium titanate pigments. Hence, a compositional variability ($0.49 < x < 0.64$) can be inferred for the synthesized $Ti_xZr_{1-x}O_4$ compounds corresponding to the compositions expected for the disordered phase [3,4] or even with a slight Ti excess, in the midway to the srilankite field.

The above results are somehow in contrast since, on one side, the shortening of the *b*-axis and the presence of exsolved $ZrO_2$ might be both regarded as indications of cation ordering within the Zr–Ti layers of doped and co-doped samples, while, on the other side, the absence of superstructure peaks in all zirconium titanate pigments and the satisfactory quality of structure refinements performed with the disordered structure model (space group *Pbcn*; setting of the unit cell: $a \cdot b \cdot c = 4.7 \cdot 5.5 \cdot 5.0$ Å) clearly

Table 2
Structural data of zirconium titanate pigments: unit-cell parameters (*a*, *b*, *c*. volume), occupancy of Zr in the octahedral site expressed as atoms per unit formula (a.p.f.u.), isotropic displacement parameters ($U_{ISO} \times 100$) and atomic positions

| Sample | *a* (Å) | *b* (Å) | *c* (Å) | Volume (Å$^3$) | Occupancy of Zr | $U_{ISO} \times 100$ | | Atomic positions | | | |
|---|---|---|---|---|---|---|---|---|---|---|---|
| | | | | | | (Zr.Ti) | (O) | *y*(Zr,Ti) | *x*O | *y*O | *z*O |
| ZT | 4.806(4) | 5.467(0) | 5.032(7) | 132.20 | 0.50(2) | 2.0(1) | 2.8(1) | 0.2007(3) | 0.2736(5) | 0.3963(3) | 0.4334(4) |
| Co | 4.820(3) | 5.421(2) | 5.034(3) | 131.53 | 0.44(2) | 3.0(1) | 3.5(1) | 0.2083(3) | 0.2777(4) | 0.3952(3) | 0.4468(5) |
| CoSb | 4.814(5) | 5.427(4) | 5.036(6) | 131.58 | 0.44(6) | 2.7(1) | 3.5(1) | 0.2043(2) | 0.2729(3) | 0.3945(5) | 0.4440(4) |
| CoW | 4.812(1) | 5.436(9) | 5.033(1) | 131.65 | 0.44(6) | 3.1(1) | 3.5(1) | 0.2011(3) | 0.2671(3) | 0.3958(4) | 0.4317(5) |
| Cr | 4.818(2) | 5.448(8) | 5.035(6) | 132.15 | 0.39(9) | 2.7(1) | 3.5(1) | 0.2040(4) | 0.2754(5) | 0.3941(4) | 0.4347(3) |
| CrSb | 4.816(1) | 5.447(9) | 5.039(1) | 132.17 | 0.38(5) | 2.4(2) | 2.7(1) | 0.2022(4) | 0.2745(5) | 0.3873(3) | 0.4357(4) |
| CrW | 4.814(3) | 5.448(0) | 5.037(7) | 132.08 | 0.37(9) | 2.8(3) | 3.5(1) | 0.2009(4) | 0.2706(5) | 0.3957(4) | 0.4354(3) |
| Fe | 4.821(8) | 5.428(1) | 5.036(7) | 131.76 | 0.47(2) | 3.0(2) | 3.5(1) | 0.2058(4) | 0.2745(7) | 0.3839(5) | 0.4443(7) |
| FeSb | 4.821(1) | 5.429(0) | 5.038(0) | 131.85 | 0.40(4) | 2.3(2) | 3.0(2) | 0.2038(5) | 0.2792(5) | 0.3880(7) | 0.4385(5) |
| FeW | 4.810(6) | 5.447(2) | 5.033(4) | 131.86 | 0.40(4) | 2.5(2) | 2.9(3) | 0.2011(4) | 0.2760(4) | 0.4023(4) | 0.4379(6) |
| Mn | 4.816(7) | 5.428(3) | 5.033(5) | 131.56 | 0.43(7) | 2.8(3) | 3.5(3) | 0.2047(5) | 0.2703(5) | 0.3987(6) | 0.4342(4) |
| MnSb | 4.811(0) | 5.449(2) | 5.036(1) | 132.02 | 0.36(6) | 2.7(3) | 3.5(3) | 0.2015(6) | 0.2706(6) | 0.3976(4) | 0.4428(6) |
| MnW | 4.809(6) | 5.444(2) | 5.032(3) | 131.76 | 0.39(3) | 3.0(2) | 3.5(2) | 0.2024(7) | 0.2721(5) | 0.3904(5) | 0.4400(4) |
| Ni | 4.820(9) | 5.425(6) | 5.034(3) | 131.65 | 0.37(7) | 2.8(2) | 3.1(2) | 0.2052(7) | 0.2731(5) | 0.3946(8) | 0.4407(7) |
| NiSb | 4.814(9) | 5.436(1) | 5.037(3) | 131.82 | 0.48(6) | 3.1(2) | 3.5(2) | 0.2032(6) | 0.2702(5) | 0.3924(4) | 0.4416(4) |
| NiW | 4.812(6) | 5.433(3) | 5.033(6) | 131.58 | 0.38(8) | 3.3(2) | 3.5(2) | 0.2025(7) | 0.2747(5) | 0.3948(5) | 0.4480(5) |
| V | 4.813(6) | 5.427(3) | 5.030(7) | 131.37 | 0.44(5) | 2.7(2) | 3.5(2) | 0.2050(7) | 0.2727(7) | 0.3933(6) | 0.4355(8) |
| VSb | 4.809(3) | 5.440(2) | 5.033(6) | 131.66 | 0.39(3) | 2.9(2) | 3.5(2) | 0.2026(8) | 0.2736(9) | 0.3958(8) | 0.4378(7) |
| VW | 4.806(4) | 5.444(7) | 5.031(5) | 131.64 | 0.51(6) | 2.1(3) | 3.5(2) | 0.1986(7) | 0.2720(6) | 0.4020(6) | 0.4160(8) |
| Pr | 4.813(0) | 5.435(7) | 5.032(4) | 131.61 | 0.40(2) | 2.9(1) | 3.2(1) | 0.2037(6) | 0.2666(6) | 0.3949(5) | 0.4414(5) |

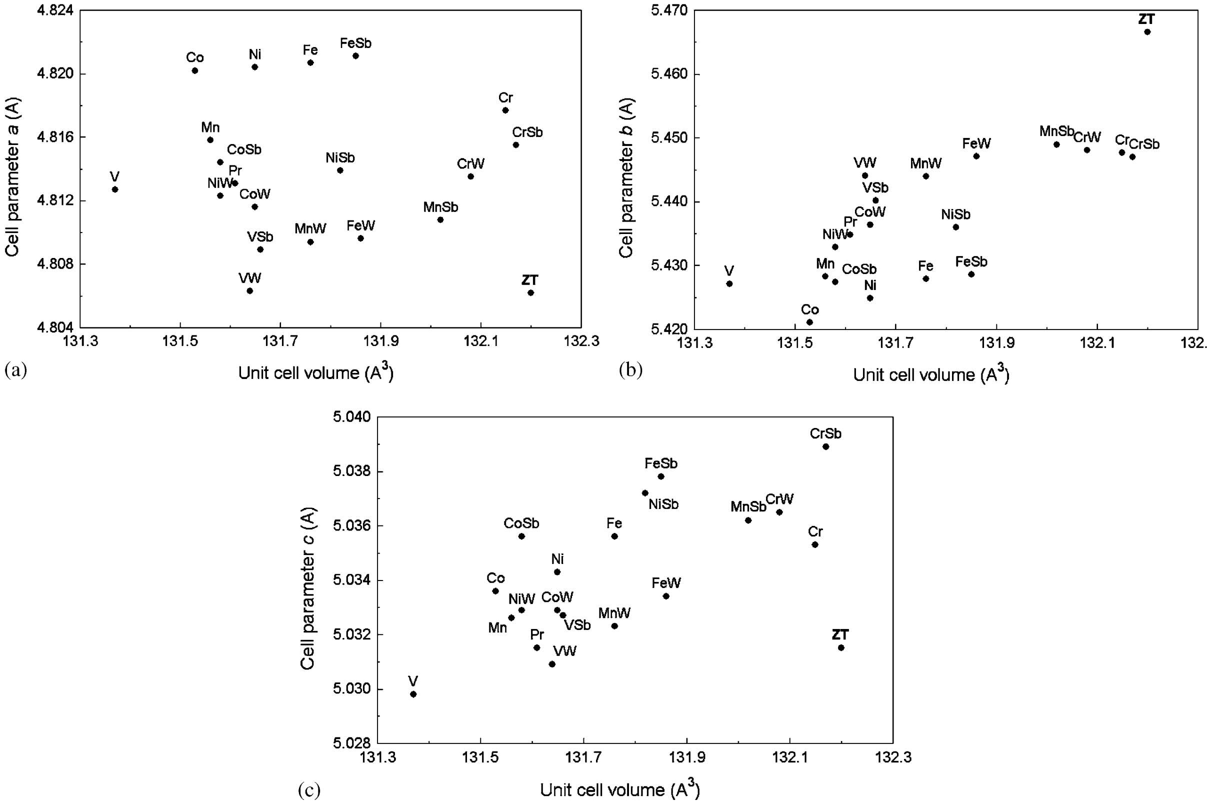

Fig. 2. Plot of the cell parameters *a*(a), *b*(b), *c*(c) vs. unit cell volume.

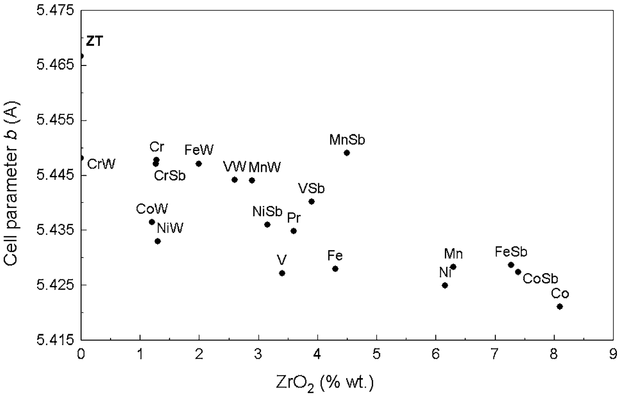

Fig. 3. Plot of the amount of the accessory phase $ZrO_2$ (expressed in % weight) vs. cell parameter *b*.

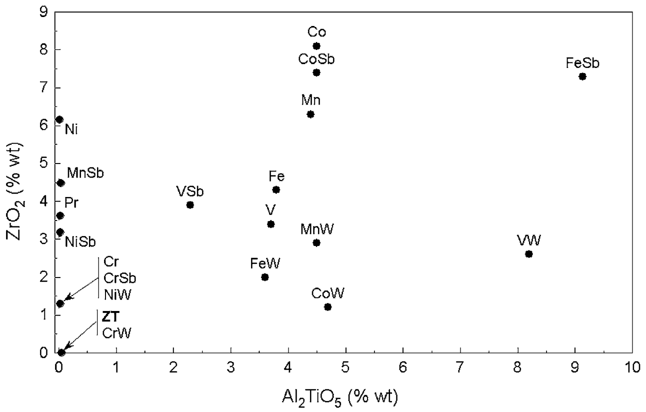

Fig. 4. Plot of the amount of the accessory phase tialite ($Al_2TiO_5$) vs. amount of the accessory phase baddeleyite ($ZrO_2$).

show that all samples retained a mainly disordered state. This situation is very similar to that reported by Sham et al. [24] for zirconium titanate samples synthesized by sol–gel method and treated at 1000 °C. The authors successfully performed crystal structure refinements based on the disordered model (no superstructure peaks were reported) while the occupancy refinements of Zr/Ti ratio and the coexistence of a $ZrO_2$ phase showed that the stoichiometry of samples was close to $Zr_5Ti_7O_{24}$, as for the ordered structure. From the above considerations, our zirconium titanate pigments are consistent with the srilankite-type structure in which the Zr/Ti disordered state coexists with a Ti-enriched stoichiometry.

## *3.2. Optical spectroscopy*

The sample ZT exhibits a weak light absorption in the violet region, probably connected with a metal–ligand charge transfer (CT) analogue to the well-known $Ti^{4+}$–$O^{2-}$ CT in rutile [12]. However, comparing the two spectra (Fig. 5), it is clear that the position of the CT band of zirconium titanate is shifted to higher energies as well as the band slope is much less inclined, thus playing minor effects on the visible range. At all events, some overlappings of CT and CF effects may occur, making more difficult the quantitative interpretation of optical spectra with measurement of CF strength (*Dq*) as well as interelectronic repulsion Racah *B* parameter. In order to enhance the resolution of CF peaks in the blue to UV range, the CT contribution was removed by systematic subtraction of the spectrum of undoped zirconium titanate.

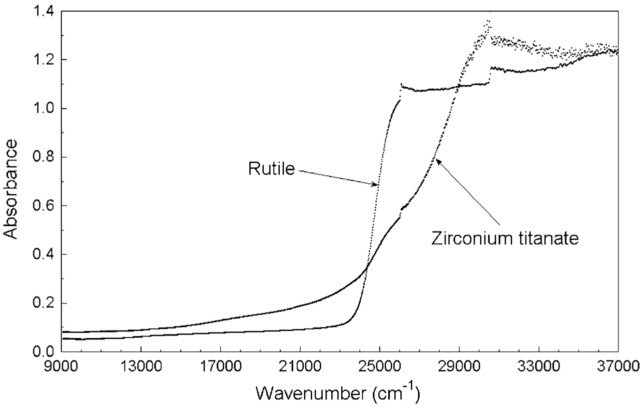

Fig. 5. UV–visible–NIR spectra of zirconium titanate and rutile.

The wavenumbers of CF peaks and band width ($\delta$), the inferred values of average (cubic) *Dq* and Racah $B_{35}$ as well as the calculated CFSE and nephelauxetic ratio ($\beta_{35}$) are listed in Table 3. For simplicity sake, CF peaks are described as the symmetry of octahedral site would be cubic, despite the point symmetry of the (Zr,Ti)O$_6$ is C$_2$. Just in case of a conspicuous peak splitting, the terminology is referred to a lower symmetry group.

### 3.2.1. Cobalt doping

Two main effects are found in the case of cobalt doping, as broad bands around 16,500 and 23,000 cm$^{-1}$, respectively, plus an absorbance increase below 10,000 cm$^{-1}$ that is likely to be the tail of a peak centred at wavenumbers just below 9000 cm$^{-1}$ (Fig. 6). All these peaks can be attributed to Co$^{2+}$ in octahedral coordination and particularly to the CF transitions: $^4T_{1g}(^4F)\rightarrow{}^4T_{2g}(^4F)$ at ~9000 cm$^{-1}$ ($\upsilon_1$), $^4T_{1g}(^4F)\rightarrow{}^4A_{2g}(^4F)$ at ~16,500 cm$^{-1}$ ($\upsilon_2$)

Table 3
Optical spectroscopic data: crystal field transitions, crystal field strength (*Dq*), crystal field stabilization energy (CFSE), Racah parameters $B_{35}$ and $\beta_{35}$

| Ion | Sample | Crystal field transitions (cm$^{-1}$) | | | Peak splitting $\delta$ (cm$^{-1}$) | *Dq* (cm$^{-1}$) | CFSE (kJ/g·ion) | Racah $B_{35}$ (cm$^{-1}$) | $\beta_{35}$ |
|---|---|---|---|---|---|---|---|---|---|
| | | $\upsilon_1$ | $\upsilon_2$ | $\upsilon_3$ | | | | | (1) |
| Co$^{2+}$ | Co | n.d. | 16,890 | 23,030 | 2740 | 898 | −86.0 | 597 | 0.60 |
| | CoSb | n.d. | 16,580 | 23,380 | 2600 | 882 | −84.4 | 686 | 0.69 |
| | CoW | n.d. | 16,450 | 23,120 | 2560 | 875 | −83.8 | 670 | 0.68 |
| Cr$^{3+}$ | Cr | 14,310 | 18,570 | n.d. | 1250 | 1425 | −204.5 | 397 | 0.43 |
| | CrSb | 14,170 | 20,390 | n.d. | 1330 | 1487 | −213.4 | 644 | 0.69 |
| | CrW | 14,100 | 19,430 | n.d. | 1320 | 1447 | −207.7 | 524 | 0.56 |
| Fe$^{3+}$ | Fe | 13,010 | 17,830 | 20,430 | | (1207) | 0 | 681 | 0.66 |
| | FeSb | n.d. | 15,600 | 21,110 | | (1407) | 0 | 704 | 0.68 |
| | FeW | 13,920 | 15,580 | 20,660 | | (1316) | 0 | 689 | 0.67 |
| Mn$^{2+}$ | Mn | 14,450 | 19,050 | 23,930 | | (1047) | 0 | 798 | 0.83 |
| | MnSb | 10,950 | 18,510 | 23,860 | | (1269) | 0 | 795 | 0.83 |
| | MnW | 14,430 | 20,130 | 24,350 | | (972) | 0 | 812 | 0.85 |
| Mn$^{3+}$ | Mn | 16,750 | | | 4600 | 1675 | −136.8 | | |
| | MnSb | 14,730 | | | 7560 | 1473 | −132.9 | | |
| | MnW | 17,280 | | | 5700 | 1728 | −144.5 | | |
| Ni$^{2+}$ | Ni | n.d. | 13,640 | 23,310 | 1540 | 879 | −135.2 | 645 | 0.62 |
| | NiSb | n.d. | 13,250 | 24,080 | 1580 | 874 | −131.4 | 722 | 0.69 |
| | NiW | n.d. | 13,320 | 23,800 | 1490 | 885 | −132.1 | 699 | 0.67 |
| V$^{3+}$ | V | 16,100 | 23,410 | n.d. | | 1696 | −162.3 | 769 | 0.87 |
| | VSb | 15,780 | 23,400 | n.d. | | 1678 | −160.7 | 828 | 0.94 |
| | VW | 16,000 | 23,740 | n.d. | | 1710 | −163.7 | 842 | 0.95 |
| V$^{4+}$ | V | 19,800 | | | | 1980 | −142.2 | | |
| | VSb | 19,540 | | | | 1954 | −140.3 | | |
| | VW | 20,040 | | | | 2004 | −143.9 | | |

Crystal field transitions: Co$^{2+}$: $\upsilon_2={}^4T_{1g}(^4F)\rightarrow{}^4A_{2g}(^4F)$, $\upsilon_3={}^4T_{1g}(^4P)$; Cr$^{3+}$: $\upsilon_1={}^4A_{2g}(^4F)\rightarrow{}^4T_{1g}(^4F)$, $\upsilon_2={}^4T_{2g}(^4F)$; Fe$^{3+}$ and Mn$^{2+}$: $\upsilon_1={}^6A_1(^6S)\rightarrow{}^4T_1(^4G)$, $\upsilon_2={}^4T_2(^4G)$, $\upsilon_3={}^4E,\ {}^4A(^4G)$; Mn$^{3+}$: $\upsilon_1={}^5E_g(^5D)\rightarrow{}^5T_{2g}(^5D)$; Ni$^{2+}$: $\upsilon_2={}^3A_{2g}(^3F)\rightarrow{}^3T_{1g}(^3F)$, $\upsilon_3={}^3T_{1g}(^3P)$; V$^{3+}$: $\upsilon_1={}^3T_1(^3F)\rightarrow{}^3T_2(^3F)$, $\upsilon_2={}^3T_1(^3P)$; V$^{4+}$: $\upsilon_1={}^2T_{2g}(^2D)\rightarrow{}^2E_g(^2D)$. Splitting is of $\upsilon_1$ (Cr, Mn) and $\upsilon_2$ (Co, Ni). Racah $\beta_{35}=B_{35}/B_0$ where $B_0$ (cm$^{-1}$). Co$^{2+}$: 989; Cr$^{3+}$: 933; Fe$^{3+}$: 1029; Mn$^{2+}$: 960; Ni$^{2+}$: 1042; V$^{3+}$: 886 [20,21]. Values in brackets are indicative.

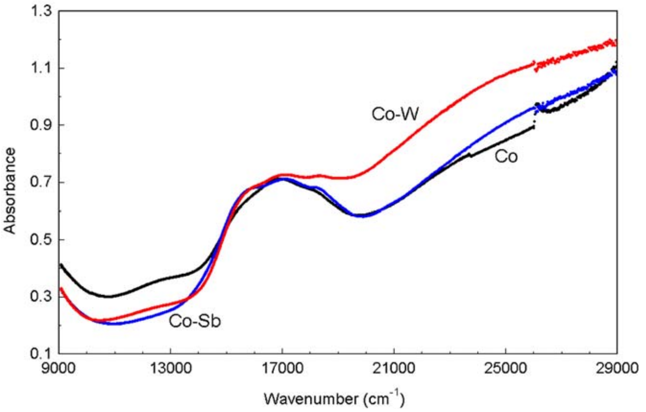

Fig. 6. UV–visible–NIR spectra of zirconium titanate pigments doped with cobalt and co-doped with counterions.

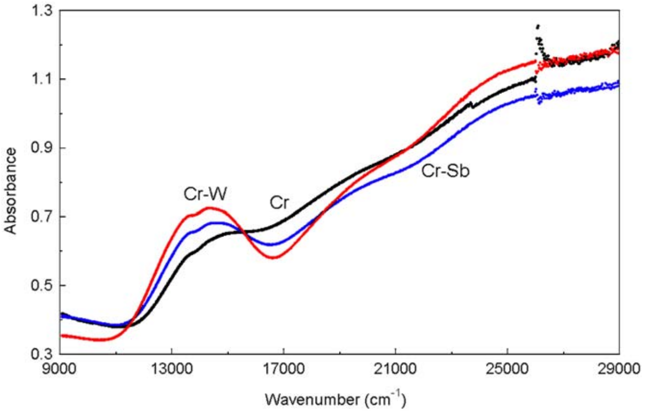

Fig. 7. UV–visible–NIR spectra of zirconium titanate pigments doped with chromium and co-doped with counterions.

and ${}^4T_{1g}({}^4F)\rightarrow{}^4T_{1g}({}^4P)$ at ~23,000 cm$^{-1}$ ($\upsilon_3$). These spectral features indicate a CF strength $Dq$ around 880 cm$^{-1}$ and $B_{35}$ values in the 600–690 cm$^{-1}$ range. The $\upsilon_2$ transition appears to be clearly threefold splitted (${}^4A\rightarrow{}^4A\ {}^4B\ {}^4B$) according to the low point symmetry of the (Zr,Ti)O$_6$ octahedron [11,12]. This splitting is as wide as ~2600 cm$^{-1}$ in the CoSb and CoW pigments and ~2750 cm$^{-1}$ in the Co sample.

### 3.2.2. Chromium doping

The occurrence of Cr$^{3+}$ into the zirconium titanate lattice generates two main parity-forbidden transitions: $\upsilon_1={}^4A_{2g}({}^4F)\rightarrow{}^4T_{1g}({}^4F)$ and $\upsilon_2={}^4A_{2g}({}^4F)\rightarrow{}^4T_{2g}({}^4F)$, that are observable as broad absorbance bands centred approximately at 14,000 and 19,000 cm$^{-1}$, respectively (Fig. 7). The CF strength varies in the 1420–1490 cm$^{-1}$ range, while the $B_{35}$ values fluctuate widely from 400 to 640 cm$^{-1}$, due to some uncertainties in deconvolving the broad $\upsilon_2$ band. The low point symmetry of the Cr$^{3+}$ site causes a threefold splitting of the $\upsilon_1$ transition, as wide as ~1300 cm$^{-1}$, with a considerable broadening of the $\upsilon_2$ peak. The enhancement of absorption by C+C doping compared with Cr doping alone could be probably due to a relaxation of the parity selection rule, though the stronger covalent character of Cr–O bonding in the Cr sample seems to be contradictory [12]. Similar spectral response was observed in rutile pigments where the Cr+W doping determined a sharper $v_1$ band at ~14,000 cm$^{-1}$; a contribution from the ${}^2E\rightarrow{}^2B_2$ transition of W$^{5+}$ was supposed [28].

### 3.2.3. Fe-doped srilankite

The spectra of iron-doped zirconium titanate present a single absorbance peak at ~20,500 cm$^{-1}$, due to the predominant ${}^6A_1({}^6S)\rightarrow{}^4E,{}^4A({}^4G)$ transition of Fe$^{3+}$ in octahedral environment ($\upsilon_3$). Further, very weak bands may be deconvolved at about 13,500 and 15,500 cm$^{-1}$, corresponding to the spin-forbidden transitions $\upsilon_1={}^6A_1({}^6S)\rightarrow{}^4T_1({}^4G)$ and $\upsilon_2={}^6A_1({}^6S)\rightarrow{}^4T_2({}^4G)$, respectively (Fig. 8).

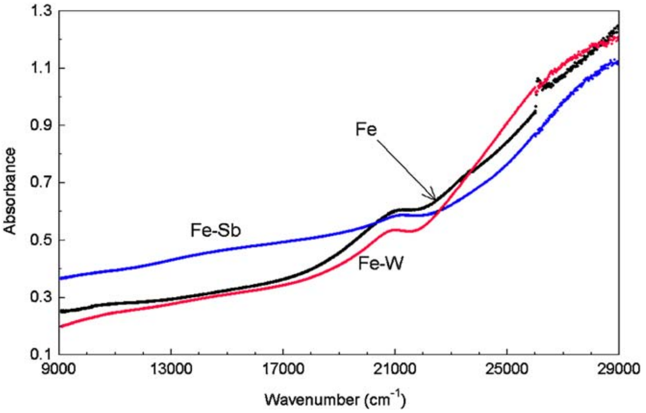

Fig. 8. UV–visible–NIR spectra of zirconium titanate pigments doped with iron and co-doped with counterions.

The DRS curves of Fe and FeW samples are very similar, while the FeSb co-doping causes an absorbance increase in the 9000–20,000 cm$^{-1}$ range, whose origin could be related to the occurrence of a significant amount of baddeleyite. In fact, this latter oxide is able to host iron (and particularly Fe$^{2+}$) inside its lattice, with increased light absorption in the red-orange region. The $Dq$ values, widely ranging in between 1200 and 1400 cm$^{-1}$, are inferred with many uncertainties due to the low definition of the spin-forbidden peaks.

### 3.2.4. Mn-doped srilankite

There is a clear difference between the spectra of Mn and MnSb on one side and that of MnW on the other: the former exhibit absorbance curves regularly increasing from NIR to UV, with two weak bands around 18,000 and 24,000 cm$^{-1}$; the latter presents a lower absorbance in the IR–visible range, with two sharper bands centred at ~14,500 and ~20,000 cm$^{-1}$, respectively

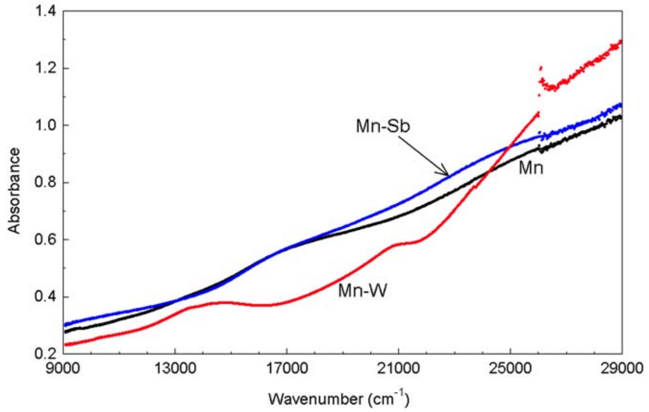

Fig. 9. UV–visible–NIR spectra of zirconium titanate pigments doped with manganese and co-doped with counterions.

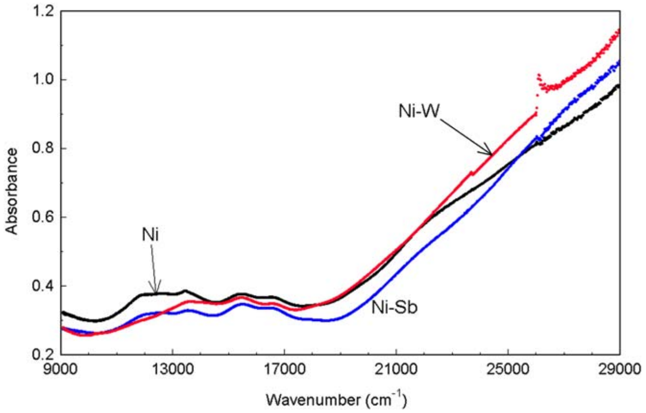

Fig. 10. UV–visible–NIR spectra of zirconium titanate pigments doped with nickel and co-doped with counterions.

(Fig. 9). These features are consistent with the occurrence of both $Mn^{2+}$ and $Mn^{3+}$ in octahedral coordination, the strong band being at ~24,000 cm$^{-1}$ attributable to the $^6A_1(^6S)\rightarrow{}^4E,^4A(^4G)$ transition of $Mn^{2+}$ ($\upsilon_3$), while the other two peaks may be interpreted as either the widely splitted transition $^5E_g(^5D)\rightarrow{}^5T_{2g}(^5D)$ of $Mn^{3+}$ in a distorted environment [12] or the spin-forbidden transitions $\upsilon_1$ and $\upsilon_2$ of $Mn^{2+}$. In the hypothesis of $Mn^{3+}$—that is the valence of manganese precursor used in our synthesis—$Dq$ would vary from 1470 to 1730 cm$^{-1}$, with a peak splitting between 4600 and 7600 cm$^{-1}$. Though a reduction to $Mn^{2+}$ during calcination was already recorded in other systems, such as $TiO_2$ [27,28], it would bring about a position of the $\upsilon_3$ band that is shifted to rather high energies. At all events, $Dq$ values, fluctuating between 970 and 1270 cm$^{-1}$, are just indicative, since the position of the very weak bands $\upsilon_1$ and $\upsilon_2$ is uncertain.

### 3.2.5. *Nickel doping*

The DRS patterns of Ni-doped zirconium titanate are similar in all samples: a complicated structure with several weak peaks characterizes the IR-to-green region, while a rapidly growing absorbance occurs from blue to the near UV (Fig. 10). These effects can be explained by CF transitions of $Ni^{2+}$ in an octahedral site, the main band being at ~24,000 cm$^{-1}$ attributable to the $\upsilon_3$ transition $^3A_{2g}(^3F)\rightarrow{}^3T_{1g}(^3P)$ and the three peaks in the 11,000–14,000 cm$^{-1}$ range to a threefold splitting of the $\upsilon_2$ transition $^3A_{2g}(^3F)\rightarrow{}^3T_{1g}(^3F)$. The further couple of peaks in the 15,000–17,000 cm$^{-1}$ interval could be due to a split spin-forbidden transition $^3A_{2g}(^3F)\rightarrow{}^1E_g(^1D)$ though its position would be expected in the green-blue region, according to the Tanabe–Sugano diagram [12]. In this framework, the weak increase of absorbance below 10,000 cm$^{-1}$ is expected to be the tail of the $\upsilon_1$ transition $^3A_{2g}(^3F)\rightarrow{}^3T_{2g}(^3F)$. This interpretation is supported by $Dq$ values (in $d^8$ configuration $10Dq = \upsilon_1$) just below 900 cm$^{-1}$. The splitting of the $\upsilon_2$ transition is about 1500 cm$^{-1}$.

### 3.2.6. *Praseodymium doping*

The substitution of praseodymium for zirconium does not produce any colouring, as it gives rise just to a very low absorbance in the entire visible range, apart from some weak peaks attributable to *f–f* transitions of the lanthanide. In contrast, the same replacement in zircon develops an intense yellow colour due to the total absorption of the violet light [29]. This different behaviour can be justified both in terms of diverse point symmetry ($C_2$ in zirconium titanate vs. $D_{2d}$ in zircon) and mean metal–oxygen distance of the Pr ion (2.047 Å in zirconium titanate instead of 2.196 Å in zircon).

### 3.2.7. *Vanadium doping*

The optical spectra exhibit a gradual increase of absorbance toward the UV region, with two weak bands around 16,000 and 23,000 cm$^{-1}$ (Fig. 11) that are referable to $V^{3+}$ in octahedral environment and particularly to the parity-forbidden transitions $\upsilon_1 = {}^3T_1(^3F)\rightarrow{}^3T_2(^3F)$ and $\upsilon_2 = {}^3T_1(^3F)\rightarrow{}^3T_1(^3P)$. Values of $Dq$ and $B_{35}$ are found to vary in a limited range: 1680–1710 cm$^{-1}$ and 770–840 cm$^{-1}$, respectively. However, these spectra cannot be successfully deconvolved unless a third band—with an intermediate wavenumber between $\upsilon_1$ and $\upsilon_2$ of $V^{3+}$—is involved. This band, centred approximately at 20,000 cm$^{-1}$, may be referred to the $^2T_{2g}(^2D)\rightarrow{}^2E_g(^2D)$ transition of $V^{4+}$ in an octahedral site that is likely to occur because the precursor is a pentavalent vanadium oxide. The occurrence of the $V^{4+}$ ion in ceramic pigments, already found in zircon and baddeleyite, gave rise to a clearly split transition, for instance 12,500 and 15,700 cm$^{-1}$ in zircon [30–32]. In any case, the very low resolution of our spectra does not allow any inference about this kind of peak splitting.

### 3.3. *Technological properties*

The chromatic performances of currently used ceramic pigments are contrasted with those of zirconium titanate pigments (Fig. 12). These latter exhibit the following

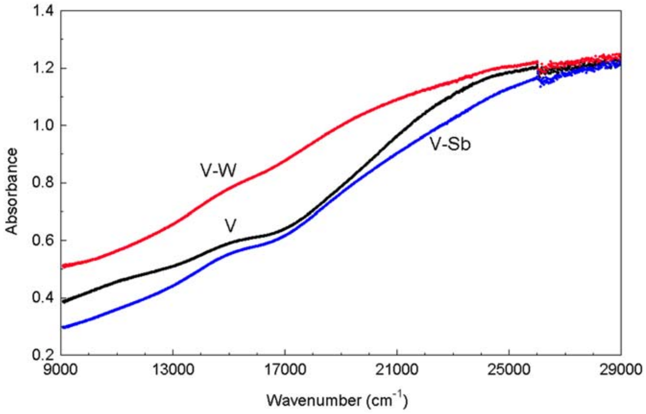

Fig. 11. UV–visible–NIR spectra of zirconium titanate pigments doped with vanadium and co-doped with counterions.

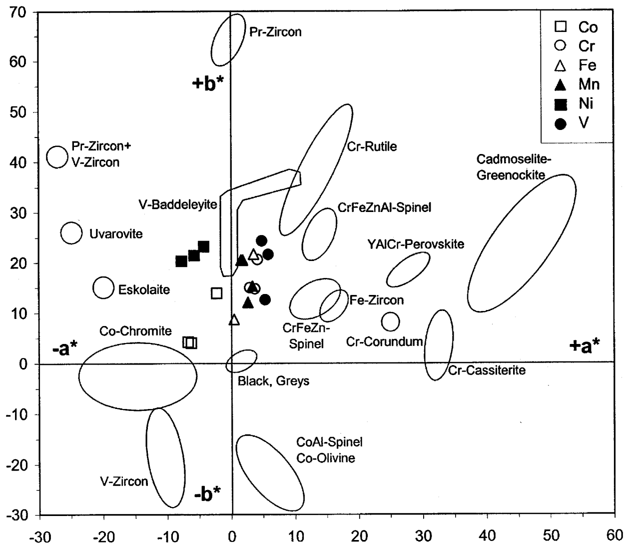

Fig. 12. Chroma plot for industrial and zirconium titanate pigments.

colours: light green (Co), greenish yellow (Ni), light brown tan (Fe and Mn), orange buff (Cr and V). All these colours are less saturated than the correspondent industrial pigments. As a matter of fact, Co and CoSb samples are quite close to the field of Co chromite, while CrW, MnW and VSb samples develop colours in between of V-zirconia and Cr-rutile. Ni samples exhibit an original green-yellow hue, however much less intense than the mixture of yellow and turquoise zircon [6,17,32]. Zirconium titanate pigments behave in a different way in low-temperature vs. high-temperature ceramic glazes and frits as well as in through-body applications. This ceramic behaviour was assessed by considering the chromatic changes in different matrices (frit, glazes, body) and temperatures (Table 4 and Fig. 13).

### 3.3.1. *Low-temperature applications*

Once the pigments are applied in a typical boric-alkaline frit, utilized for ceramic products fired at low temperatures (e.g. double-fired porous tiles, earthenware and majolica tableware), the colour achieved at 950 °C is the same of the Co-, Mn- and Ni-doped zirconium titanate, while the orange-buff hue of Cr- and V-bearing pigments is even enhanced in saturation once dispersed into the glass.

The behaviour of zirconium titanate in the chemically aggressive environment of the molten frit—rich in lead, zinc, and magnesium among others—is rather good for Cr, Mn and V samples, that do not change appreciably their colour increasing the firing temperature to 1000 °C. In the same condition, a colour virage (from green to light brown) occurs in the case of frit containing Co- and Ni-doped pigments.

### 3.3.2. *High-temperature glazes*

The thermal stability of zirconium titanate appears to be dramatically reduced in ceramic applications such as glazed tiles, that couple high temperature (from 1100 to over

Table 4
Colourimetric characteristics of selected srilankite pigments dispersed in ceramic glazes (F1: double-firing frit; S3: monoporosa glaze; S2: stoneware glaze; S1; porcelain stoneware glaze) and in a porcelain stoneware body (G) and fired at different maximum temperatures (T) for annealing times of 5–10 min

| Pigment | F1 ($T = 930\,°C$) | | | F1 ($T = 1000\,°C$) | | | S3 ($T = 1100\,°C$) | | | S2 ($T = 1150\,°C$) | | |
|---|---|---|---|---|---|---|---|---|---|---|---|---|
| | $L^*$ | $a^*$ | $b^*$ | $L^*$ | $a^*$ | $b^*$ | $L^*$ | $a^*$ | $b^*$ | $L^*$ | $a^*$ | $b^*$ |
| CoSb | 64.20 | −6.83 | 6.05 | 84.69 | 1.11 | 7.94 | 79.34 | −3.59 | −1.98 | 72.57 | −3.12 | −4.91 |
| CrW | 63.18 | 6.11 | 29.59 | 70.47 | 5.26 | 33.59 | 78.81 | 3.38 | 12.45 | 80.68 | 2.13 | 15.38 |
| MnW | 66.51 | 5.88 | 19.91 | 71.90 | 5.43 | 20.09 | 83.60 | 2.31 | 10.93 | 84.44 | 2.20 | 12.40 |
| NiSb | 83.42 | −2.73 | 23.20 | 87.50 | 0.33 | 17.94 | 89.41 | 0.03 | 10.49 | 86.31 | 1.12 | 11.99 |
| V | 59.22 | 8.04 | 31.10 | 64.78 | 8.55 | 31.89 | 82.12 | 3.01 | 18.97 | 85.06 | 2.29 | 15.14 |

| Pigment | S1 ($T = 1200\,°C$) | | | S1 ($T = 1250\,°C$) | | | G ($T = 1200\,°C$) | | | G ($T = 1250\,°C$) | | |
|---|---|---|---|---|---|---|---|---|---|---|---|---|
| | $L^*$ | $a^*$ | $b^*$ | $L^*$ | $a^*$ | $b^*$ | $L^*$ | $a^*$ | $b^*$ | $L^*$ | $a^*$ | $b^*$ |
| CoSb | 73.28 | −2.31 | −0.71 | 66.18 | −1.39 | −11.50 | 79.88 | −1.75 | 6.05 | 79.38 | −2.21 | 5.83 |
| CrW | 76.56 | 0.93 | 18.33 | 73.19 | −1.53 | 15.11 | 80.13 | 1.56 | 12.84 | 80.28 | 1.53 | 12.97 |
| MnW | 79.69 | 1.87 | 13.78 | 81.39 | 1.21 | 11.46 | 82.79 | 1.28 | 10.52 | 81.36 | 0.95 | 11.26 |
| NiSb | 82.40 | 0.75 | 13.54 | 81.59 | 1.06 | 13.27 | 85.21 | 0.49 | 9.66 | 83.34 | −0.04 | 9.90 |
| V | 80.29 | 2.21 | 17.55 | 80.13 | 1.53 | 12.82 | 81.25 | 1.30 | 17.10 | 76.53 | 1.60 | 18.03 |

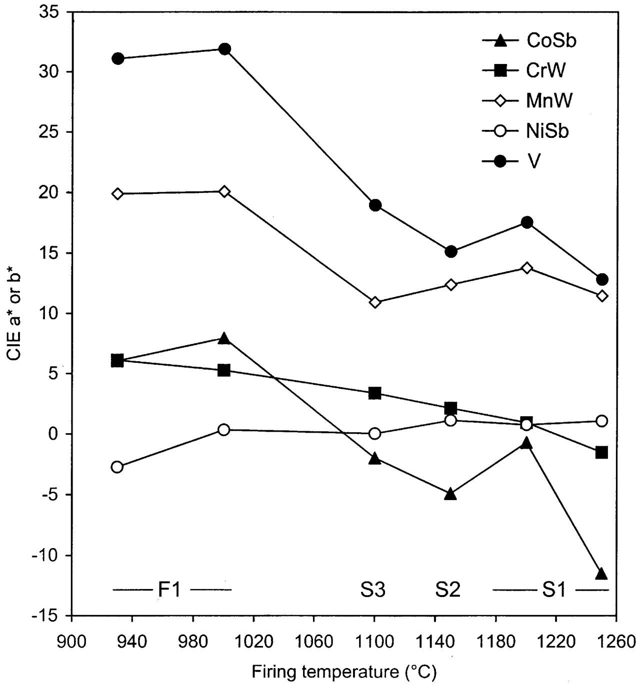

Fig. 13. Colour change (*a** for Cr- and Ni-doped, *b** for Co-, Mn- and V-doped) vs. maximum firing temperature of zirconium titanate pigments applied in frit (F1) and glazes (S1, S2 and S3).

1200 °C) with very aggressive chemical environments, due in particular to high concentrations of calcium, zinc and magnesium into the molten glaze. Zirconium titanate is partially decomposed in *monoporosa* or stoneware firing conditions, so that its colour fades in every case to a light brown hue. Exception is made of glazes containing the Co pigment, which become gradually bluer at increasing firing temperatures; in this case, the breakdown of zirconium titanate makes it available an increasing amount of $Co^{2+}$ dissolved in silicate melt, where it imparts a well-known blue coloration to silicate glass, a phenomenon known as "cobalt bleeding" [33,34].

### 3.3.3. Through-body applications

The pigment dispersion in an opaque medium, such as a porcelain stoneware body, brings about both a colour dilution and contamination by the light yellow hue of the ceramic matrix. These phenomena account for the consistent reduction of colour saturation occurring in coloured bodies, when compared to the correspondent zirconium titanate pigments, and the shift toward the colour of the undoped body (Fig. 14). Within this general trend, the Co and V pigments appear to be more resistant to the attack of the liquid phase developed at the high temperature of porcelain stoneware firing (1200–1250 °C) because the colours of bodies are still relatively close to those of pigments. In contrast, zirconium titanates containing Ni, Mn or Cr are heavily attacked by the liquid phase, since their coloration approaches that of the undoped body.

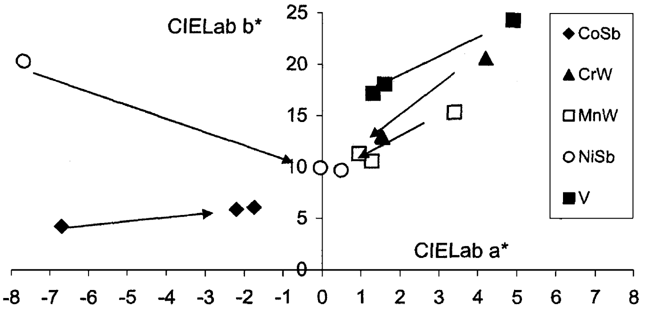

Fig. 14. Colour change of zirconium titanate pigments applied in porcelain stoneware body.

## 4. Discussion

As previously described, the results of crystal structure analysis suggest that all the studied srilankite-type pigments are characterized by an essentially disordered structure, although the shortening of the *b*-axis in doped and co-doped samples could be taken as an indication for a progressively increased degree of Zr–Ti ordering. Assuming that the variation of the *b*-axis is mainly (or only) controlled by the order/disorder kinetics, the combination of diffraction and spectroscopic data can be used to explain the quite regular variation of the *c*-axis as being proportional to the ionic radii differences (Fig. 2c). In fact, spectroscopy data revealed the following valences for the different chromophore ions (Shannon [35] ionic radii in parentheses): $Co^{2+}$ (0.75 Å), $Cr^{3+}$ (0.62 Å), $Fe^{3+}$ (0.65 Å), $Mn^{2+}$ (0.83 Å) and $Mn^{3+}$ (0.65 Å), $Ni^{2+}$ (0.69 Å), $V^{3+}$ (0.64 Å) and $V^{4+}$ (0.58 Å). By considering these valences for each ion, it is expected that the $Cr^{3+}$, $Fe^{3+}$ substitution for $Ti^{4+}$ (0.61 Å) and the $Co^{2+}$, $Mn^{2+}$ substitution for $Zr^{4+}$ (0.72 Å) would increase the *c*-axis length, while the $V^{4+}$ substitution for $Ti^{4+}$ and the $Ni^{2+}$ substitution for $Zr^{4+}$ would shorten the *c*-axis. The expected variations are actually confirmed by the unit cell modifications from XRD, with the only exception of Ni-doped samples. Regarding the C+C series, it can be observed in Fig. 2 that W generally induces a decreasing of both the *a*- and *c*-axis, while the Sb co-doping determines a decrease of the *a* cell parameter and a lengthening of the *c*-axis. Simply based on these considerations, the presence of $W^{5+}$ (0.62 Å) or $W^{6+}$ (0.60 Å) and $Sb^{3+}$ (0.76 Å) can be inferred from the refined unit cell parameters. The inferred trivalent state of Sb ions, however, disagrees with the assumption that $Sb^{5+}$, similarly to $W^{5+}$, would balance $Cr^{3+}$, $Mn^{3+}$, $Fe^{3+}$ and $V^{3+}$ in replacement of $Ti^{4+}$. In the case of $Sb^{3+}$ incorporation, the charge balance could be accomplished through a mechanism of oxygen vacancies. Therefore, we suggest that charge mismatch is compensated by counterion substitution only in the case of W addition, while samples co-doped with Sb should present anion vacancies. This latter hypothesis would require additional investigation, for instance, by neutron diffraction, to be supported. The valence of doping and co-doping ions is likely to remarkably affect the presence and amount of impurity phases. In fact, DRS spectroscopy suggests unexpected valences for Ni, Mn and Co ions ($Ni^{2+}$, $Mn^{2+,3+}$ and $Co^{2+}$) replacing $Zr^{4+}$, compared to the predicted ones ($Ni^{3+}$, $Mn^{2+}$ and $Co^{3+}$) in substitution of $Ti^{4+}$. This would lead to a batch enrichment in $ZrO_2$ that would crystallize as baddeleyite. The different amount of accessory phases from the series C with respect to the series C + C is due to the fact that $W^{5+}$ or $W^{6+}$ substitutes $Ti^{4+}$ while $Sb^{3+}$ substitutes $Zr^{4+}$, therefore co-doping with Sb should lead to higher amounts of $ZrO_2$.

Concerning the coordination environment around the chromophore ions, the results from structure refinements provide an average picture which might be significantly different from the local situation around the absorbing ion, as inferred from spectroscopy. However, it is of some interest to compare this long- and short-range information. The refined mean metal–oxygen distances are practically the same in all samples, but apical (M–O2) and equatorial (M–O1, M–O3) lengths of the $(Ti,Zr)O_6$ octahedron are very different, bringing about an increased distortion. In reality, it is more likely that each cation would occupy the octahedron with its own bond lengths, according to a model of partial relaxation of the zirconium titanate lattice [22,36]. More in detail, the doping with elements acting as chromophores or counterions causes elongation of $(Ti,Zr)O_6$ octahedra and increases the degree of distortion, compared to ZT, with the exception of samples VW and FeW (Fig. 15). The C series exhibits an elongation of the apical distance (M–O2) and a shortening of the mean equatorial metal–oxygen distances. The co-doping with W determines a flattening of the octahedra, except sample MnW, while concerning equatorial distances the variations were not relevant in most cases, except the considerable shortening in samples VW and FeW. Antimony addition brings about a wider range of situations; in fact, it determines an elongation of the octahedra in samples NiSb and CrSb, while in the other samples it is not easy to outline a unique trend concerning both the apical and equatorial distances.

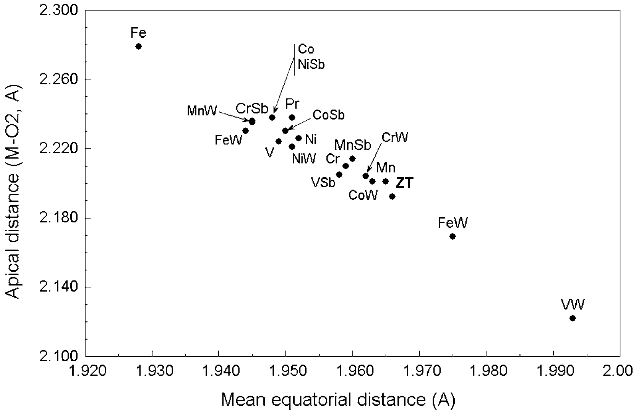

Fig. 15. The mean equatorial metal oxygen distances vs. the apical distances (M–O2).

The spectroscopic data are generally consistent with the above structural characteristics of zirconium titanate pigments; in fact, the CF theory predicts that the optical adsorptions occur at energies that are dependent on the CF strength $Dq$ and the mean metal–ligand distance $R$, according to the relationship:

$$10Dq = 5q\langle r^4\rangle\langle R\rangle^{-n},$$

where $q$ is the effective charge on the ligands, $\langle r^4 \rangle$ is the mean of the fourth power of $d$-electron–core distance, $\langle R \rangle$ is the mean metal–oxygen distance in the octahedron, and $n$ is an exponent, widely varying between 2 and 9, that is theoretically equal to 5 in the point charge model approximation [12,37].

Literature data of $Dq$ and $\langle R \rangle^{-5}$, measured on several oxides and silicates, are contrasted in Fig. 16 for the various chromophores [11]. It results that $Dq$ values of zirconium titanate pigments are at wavenumbers reasonably predicted by the CF theory on the basis of their $\langle R \rangle^{-5}$. In contrast, comparing the C and C + C series, no significant dependence of $Dq$ and $\langle R \rangle$ seems to arise, the maximum variation in most cases being $< 50\,cm^{-1}$ and $< 0.5\,pm$, respectively. Account must be taken that our spectroscopic measurements have an insufficient sensibility to small differences of $Dq$. Moreover, X-ray diffraction determines an averaged value of $\langle R \rangle$ that is known to be significantly different from the real value for the chromophore ion [22,37].

A threefold splitting of CF peaks is expected due to the low point symmetry ($C_2$) of the chromophore in the distorted octahedral site of zirconium titanate. It is possible to observe this splitting in $\nu_1$ peaks of $Cr^{3+}$ (and perhaps $Mn^{3+}$) as well as in $\nu_2$ bands of $Ni^{2+}$ and $Co^{2+}$. The full-width at half-maximum of these bands ($\delta$, Table 3) is actually proportional to the degree of distortion of the octahedron ($\Delta_6$, Table 5) in the case of Co-, Cr- and Ni-doped pigments, but for CrW. In particular, the $Mn^{3+}$ band exhibits a very wide splitting ($> 4600\,cm^{-1}$) that may be tentatively related to the well-known Jahn–Teller effect of this ion in distorted sites, besides the very scarcely resolved optical spectrum.

The nephelauxetic ratio $\beta_{35}$ increases with the addition of W and further with Sb, suggesting an increasing ionicity degree of the chromophore–oxygen bonding in presence of counterions.

## 5. Conclusions

Zirconium titanate can be coloured with first row transition elements, giving rise to different colours depending on the metal used. In industrial-like synthesis conditions, zirconium titanate has a srilankite-type disordered structure, where Ti and Zr are randomly distributed in a unique octahedral site and the phase composition is enriched in Ti.

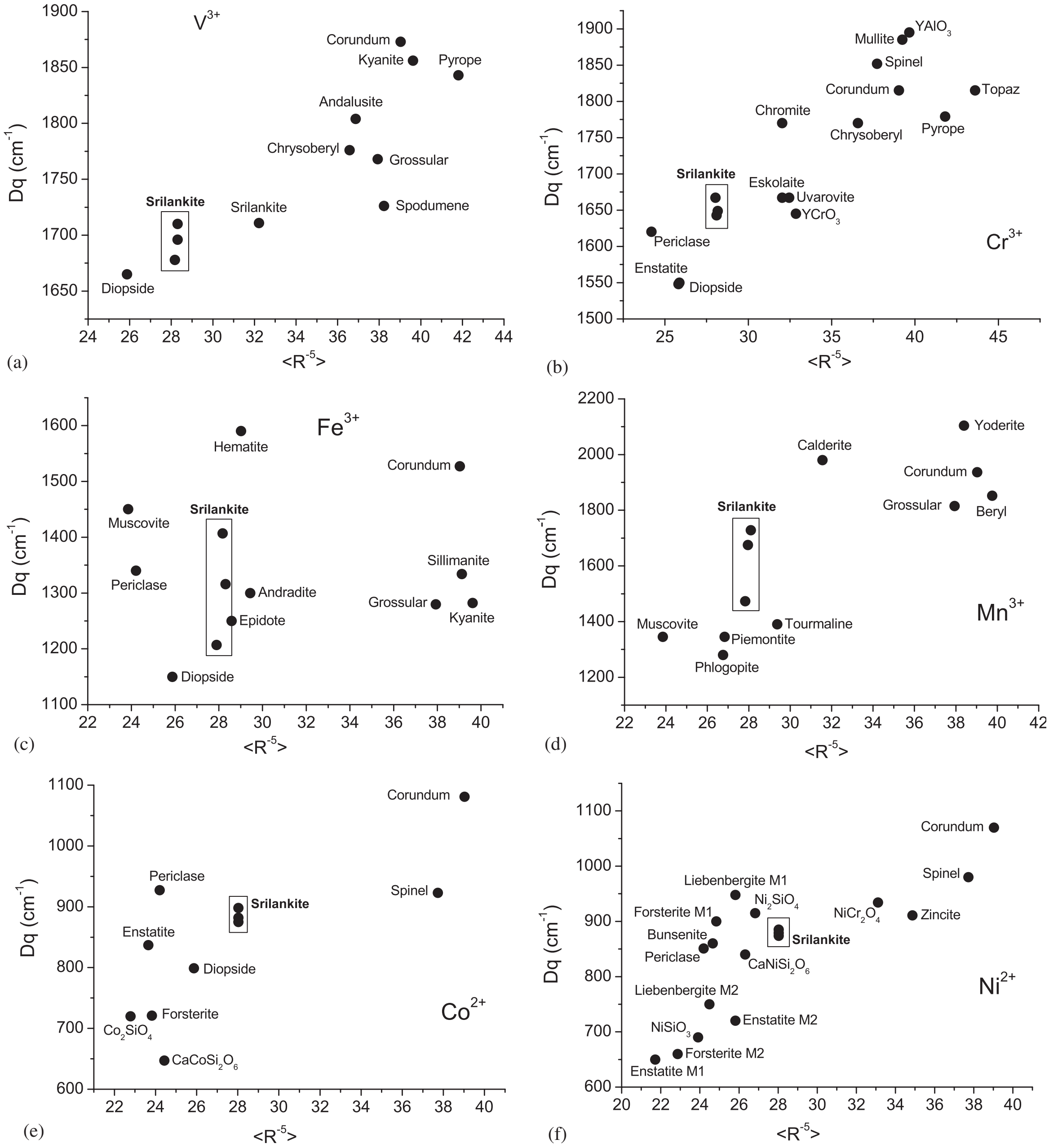

Fig. 16. Relationship between crystal field strength $Dq$ and the metal–oxygen distance $\langle R \rangle^{-5}$ for zirconium titanate and industrial ceramic pigments.

The addition of chromophores (Co, Cr, Fe, Mn, Ni, Pr or V) induces a cell volume contraction mainly due to the strong shortening of the *b*-axis, which is possibly caused by an increasing degree of ordering (at the short range) while the average structure maintains a disordered state. The shortening of the *b*-axis is accompanied by a slight lengthening of the *c* and *a* unit-cell parameters. These variations are not fully consistent with an averaged ionic radius, calculated by assuming the ion oxidation state and occupancy within the octahedral site. Associated to the unit-cell variations, the refined metal–oxygen distances and distortion degree of the (Zr,Ti)$O_6$ octahedron vary across the series in such a way that any change in the apical M–O bond length seems to be counterbalanced by an opposite change of the equatorial ones. It follows that the averaged M–O distances are almost the same in all pigments but with a different distortion degree.

Doping of zirconium titanate promotes an exsolution of $ZrO_2$, mainly due to the stoichiometry shift of the Zr:Ti ratio from 1:1 to nearly 1:2 of the srilankite-type phase but also related to the presence of $Al_2O_3$ impurity. Accordingly, coloured srilankite is almost sistematically associated with baddeleyite. When Sb or W counterions are added, in order to ensure the charge neutrality of the structure, it appears that different charge balancing mechanisms are operating: formation of anion vacancies seems to be present in the former case while a coupled heterovalent substitution is acting in the latter. This implies that only

Table 5
Metal–oxygen distances and degree of distortion of the octahedral site in zirconium titanate pigments

| | (Ti,Zr)–O distances (Å) | | | | Site distortion |
|---|---|---|---|---|---|
| | Apical distances | Equatorial distances | | Mean of the 6 distances | |
| | *M*–O2 [× 2] | *M*–O1 [× 2] | *M*–O3 [× 2] | ⟨*M*–O⟩ | $\Delta_6$ |
| ZT | 2.192(5) | 1.930(5) | 2.001(5) | 2.041 | 2.94 |
| Co | 2.238(4) | 1.947(4) | 1.949(4) | 2.045 | 4.47 |
| CoSb | 2.230(4) | 1.935(4) | 1.964(4) | 2.043 | 4.22 |
| CoW | 2.201(4) | 1.900(4) | 2.025(4) | 2.042 | 3.66 |
| Cr | 2.210(4) | 1.923(4) | 1.994(4) | 2.042 | 3.57 |
| CrSb | 2.235(5) | 1.908(5) | 1.981(4) | 2.041 | 4.71 |
| CrW | 2.204(5) | 1.922(5) | 2.002(4) | 2.043 | 3.37 |
| Fe | 2.279(4) | 1.909(4) | 1.946(4) | 2.045 | 6.62 |
| FeSb | 2.230(5) | 1.927(5) | 1.961(5) | 2.039 | 4.42 |
| FeW | 2.169(4) | 1.964(4) | 1.986(4) | 2.040 | 2.03 |
| Mn | 2.201(5) | 1.914(5) | 2.016(5) | 2.044 | 3.38 |
| MnSb | 2.214(5) | 1.944(5) | 1.975(5) | 2.044 | 3.48 |
| MnW | 2.236(5) | 1.917(5) | 1.973(5) | 2.042 | 4.64 |
| Ni | 2.226(5) | 1.926(4) | 1.978(5) | 2.043 | 4.10 |
| NiSb | 2.238(5) | 1.919(4) | 1.977(4) | 2.045 | 4.60 |
| NiW | 2.221(4) | 1.949(5) | 1.953(5) | 2.041 | 3.89 |
| V | 2.224(4) | 1.904(4) | 1.994(4) | 2.041 | 4.36 |
| VSb | 2.205(5) | 1.931(4) | 1.985(4) | 2.040 | 3.37 |
| VW | 2.122(4) | 1.905(4) | 2.081(5) | 2.036 | 2.14 |
| Pr | 2.238(3) | 1.911(3) | 1.991(3) | 2.041 | 4.62 |

*Note*: $\Delta_6$ is the distortion parameter of the octahedra and is calculated as $[1/3 \times 10^3[\Sigma i(M\text{–O1}-\langle M\text{–O}\rangle)^2+(M\text{–O}_i-\langle M\text{–O}\rangle)^2]/[\langle M\text{–O}\rangle]^2]$.

tungsten addition actually increases the Zr solubility in the zirconium titanate phase.

Optical spectroscopy indicates the occurrence of the following valences: $Co^{2+}$, $Cr^{3+}$, $Fe^{3+}$, $Mn^{2+}$, $Mn^{3+}$, $Ni^{2+}$, $V^{3+}$, $V^{4+}$. There is a reasonable agreement between *Dq* and metal–oxygen distance, as predicted by the CF theory. The effect of counterions on *Dq* is scarce, but a clear influence on $B_{35}$ arose, implying a reduced covalent character of M–O bonding when Sb or W are added. However, the colour of pigments changes significantly upon the addition of a counterion with a complex dependence on *Dq* and *B*, not generalizable.

Zirconium titanate pigments exhibit different technological properties depending on the chromophore and on the different ceramic applications, where interesting green (Co), greenish-yellow (Ni) and orange-buff hues (V, Cr, Mn) are obtained. The colour development and stability is excellent in low-temperature applications, such as glazes for double-fired wall tiles, majolica and earthenware. The technological performance of zirconium titanate is clearly reduced in high-temperature applications (such as body and glazes for porcelain stoneware) or especially in strongly aggressive molten glazes (such as those rich in CaO, ZnO and MgO used in *monoporosa* and stoneware tile decoration). At all events, the behaviour of srilankite-based pigments is not suitable for through-body applications.

The colouring performance of zirconium titanate pigments appears to be worse than expected on the basis of general CF considerations, taking into account the presence of a unique octahedral site with a low point symmetry. The scarce colouring properties obtained seem to be connected with: simultaneous occurrence of multiple valences, absence of CT effects, large CF splitting due to site distortion and occurrence of local situations where the chromophore ion is hosted.

## References

[1] A. Cocco, G. Torriano, Ann. Chim. (Rome) 55 (3) (1965) 153–163.
[2] A.E. McHale, R.S. Roth, J. Am. Ceram. Soc. 66 (2) (1983) C18–C20.
[3] A.E. McHale, R.S. Roth, J. Am. Ceram. Soc. 69 (11) (1986) 827–832.
[4] U. Troitzsch, D.J. Ellis, Eur. J. Miner. 16 (2004) 577–584.
[5] R. Christoffersen, P.K. Davies, J. Am. Ceram. Soc. 75 (1992) 563–569.
[6] Y. Park, Y. Kim, Mater. Res. Bull. 31 (1996) 7–15.
[7] P. Bourder, A.E. McHale, A. Santoro, R.S. Roth, J. Am. Ceram. Soc. 69 (1986) 827–832.
[8] A. Willgallis, H. Hartl, Z. Kristall. 164 (1983) 59–66.
[9] R.E. Newnham, J. Am. Ceram. Soc. 50 (1967) 216.
[10] F. Hund, Z. Anor. Allg. Chem. 525 (1985) 221–229.
[11] R.G. Burns, Mineralogical Applications of Crystal Field Theory, second ed, Cambridge University Press, Cambridge, 1993.
[12] S. Marfunin, Physics of Minerals and Inorganic Materials, Springer, Berlin, Heidelberg, New York, 1979.
[13] Y. Zhang, P.K. Davies, J. Am. Ceram. Soc. 77 (1994) 743–748.
[14] A. Siggel, M. Jansen, Z. Anor. Allg. Chem. 58 (1990) 93–102.
[15] C.E.F. Costa, S.C.L. Crispim, S.J.G. Lima, C.A. Paskocimas, E. Longo, V.J. Fernandes Jr., A.S. Araújo, I.M.G. Santos, A.G. Souza, J. Therm. Anal. Calorim. 75 (2004) 467–473.
[16] R.A. Eppler, Am. Ceram. Soc. Bull. 66 (1987) 1600–1604.
[17] Italian Ceramic Society, Colour, Pigments and Colouring in Ceramics, Modena, SALA, 2003.

[18] A.C. Larson, R.B. Von Dreele, Los Alamos National Laboratory Report LAUR 86 (2000) 748.
[19] H. Toby, J. Appl. Crystallogr. 34 (2001) 210–213.
[20] A.B.P. Lever, Inorganic Electronic Spectroscopy, second ed, Elsevier, Amsterdam, 1984.
[21] M. Wildner, M. Andrut, C.Z. Rudowicz, in: A. Beran, E. Libowitzky (Eds.), Optical Absorption Spectroscopy in Geosciences, Part I: Basic Concepts of Crystal Field Theory, EMU Notes in Mineralogy, vol. 6, Eotvos University Press, 2004, p. 93.
[22] M. Andrut, M. Wildner, C.Z. Rudowicz, in: A. Beran, E. Libowitzky (Eds.), Optical Absorption Spectroscopy in Geosciences, Part II: Quantitative Aspects of Crystal Fields, EMU Notes in Mineralogy, vol. 6, Eotvos University Press, 2004, p. 145.
[23] F. Matteucci, C. Lepri Neto, M. Dondi, G. Cruciani, G. Baldi, A.O. Boschi, Adv. Appl. Cer. 105 (2006) 1–8.
[24] E.L. Sham, M.A.G. Aranda, E.M. Farfan-Torres, J.C. Gottifredi, M. Martinez-Lara, S. Bruquet, J. Solid State Chem. 139 (1998) 225–232.
[25] Y. Park, J. Mater. Sci. Lett. 14 (1995) 873–875.
[26] S.A.T. Redfern, in: S.A.T. Redfern, M. Carpenter (Eds.), Transformation Processes in Minerals, Mineral Society of America, Washington, DC, 2000, p. 105.
[27] J. Maloney, in: H.M. Smith (Ed.), High Performance Pigments, Wiley-VCH, 2002, p. 53.
[28] M. Dondi, G. Cruciani, G. Guarini, F. Matteucci, M. Raimondo, Ceram. Int., 2006, in press.
[29] J.A. Badenes, J.B. Vicent, M. Llusar, M.A. Tena, G. Monros, J. Mater. Sci. 37 (2002) 1413–1420.
[30] S. Di Gregorio, M. Greenblatt, J.H. Pifer, M.D. Sture, J. Chem. Phys. 76 (1982) 2931–2937.
[31] M. Ocana, A.R. Gonzalez-Elipe, V.M. Orera, P. Tartaj, C.J. Serna, J. Am. Ceram. Soc. 81 (1998) 395–400.
[32] M. Khan, Interceram 51 (2002) 212–213.
[33] R.G.V. Hancock, J. McKechnie, S. Aufreiter, K. Karklins, M. Kapches, M. Sempowski, J.F. Moreau, I. Kenyon, J. Radioanal. Nucl. Chem. 244 (2000) 567–573.
[34] R.A. Eppler, in: R.E. Kirk, D.F. Othmer (Eds.), Encyclopedia of Chemical Technology, vol. 6, Interscience, New York, 1993, p. 877.
[35] R.D. Shannon, Acta Crystallogr. A 32 (1976) 751–767.
[36] V.S. Urusov, J. Solid State Chem. 98 (1992) 223–236.
[37] K. Langer, Z. Krist. 216 (2001) 87–91.